Nucleic Acids Research, 2018 **1**
doi: 10.1093/nar/gky1215

RNA–DNA fibers and polygons with controlled immunorecognition activate RNAi, FRET and transcriptional regulation of NF-κB in human cells

Weina Ke[1], Enping Hong[2], Renata F. Saito[3], Maria Cristina Rangel[3], Jian Wang[4], Mathias Viard[5], Melina Richardson[1], Emil F. Khisamutdinov[6], Martin Panigaj[7], Nikolay V. Dokholyan[4], Roger Chammas[1,3], Marina A. Dobrovolskaia[2] and Kirill A. Afonin[1,8,*]

[1]Nanoscale Science Program, Department of Chemistry, University of North Carolina at Charlotte, Charlotte, NC 28223, USA, [2]Nanotechnology Characterization Lab., Cancer Research Technology Program, Frederick National Laboratory for Cancer Research sponsored by the National Cancer Institute, Frederick, MD 21702, USA, [3]Centro de Investigação Translacional em Oncologia (LIM24), Departamento de Radiologia e Oncologia, Faculdade de Medicina da Universidade de São Paulo and Instituto do Câncer do Estado de São Paulo, São Paulo, SP, Brazil, [4]Department of Pharmacology, Department of Biochemistry & Molecular Biology, Penn State College of Medicine, Hershey, PA 17033, USA, [5]Basic Science Program, Cancer and Inflammation Program, Leidos Biomedical Research Inc., Frederick National Laboratory for Cancer Research, Frederick, MD 21702, USA, [6]Department of Chemistry, Ball State University, Muncie, IN 47306, USA, [7]Institute of Biology and Ecology, Faculty of Science, Pavol Jozef Safarik University in Kosice, Kosice, Slovak Republic and [8]The Center for Biomedical Engineering and Science, University of North Carolina at Charlotte, Charlotte, NC 28223, USA

Received August 20, 2018; Revised November 19, 2018; Editorial Decision November 20, 2018; Accepted November 22, 2018

ABSTRACT

Nucleic acid–based assemblies that interact with each other and further communicate with the cellular machinery in a controlled manner represent a new class of reconfigurable materials that can overcome limitations of traditional biochemical approaches and improve the potential therapeutic utility of nucleic acids. This notion enables the development of novel biocompatible 'smart' devices and biosensors with precisely controlled physicochemical and biological properties. We extend this novel concept by designing RNA–DNA fibers and polygons that are able to cooperate in different human cell lines and that have defined immunostimulatory properties confirmed by *ex vivo* experiments. The mutual intracellular interaction of constructs results in the release of a large number of different siRNAs while giving a fluorescent response and activating NF-κB decoy DNA oligonucleotides. This work expands the possibilities of nucleic acid technologies by (i) introducing very simple design principles and assembly protocols; (ii) potentially allowing for a simultaneous release of various siRNAs together with functional DNA sequences and (iii) providing controlled rates of reassociation, stabilities in human blood serum, and immunorecognition.

INTRODUCTION

Various nucleic acids that are natural, rationally designed, or selected by directed evolution can be used to manipulate biological systems and therapeutically utilized to downregulate gene expression (e.g. siRNAs), target receptors (e.g. aptamers), cleave RNAs (e.g. ribozymes), or antagonize transcription (e.g. DNA decoys) (1–3). The potential of therapeutic nucleic acids (TNAs) becomes apparent from a recent inspiring example of the very first RNA interference therapeutic agent approved by FDA (4) and from many studies showing versatility, programmability, and modularity of TNAs (5–7). In addition, TNAs have intrinsic immunomodulatory properties based on the ability of human cells to discriminate self from non-self oligonucleotides and trigger innate immune responses. The size, sequence and composition of TNAs contribute to their immunorecognition (8). While the level of immune response can adversely affect the therapeutic benefit of applied TNAs, the controlled immunostimulation by nucleic acids can be used synergistically as an adjuvant (9,10). Due to the programmability of RNA and DNA, we can design their nanoassemblies with controllable physicochemical and immunogenic potential (11–18). Recently, we demonstrated that the com-

---

[*] To whom correspondence should be addressed. Tel: +1 704 687 0685; Fax: +1 704 687 0960; Email: kafonin@uncc.edu

position of nucleic acid nanoparticles (NANPs) affects the outcome of their immune response (11,12), and while RNA NANPs stimulate the production of interferons and some pro-inflammatory cytokines, we found that DNA analogs, in most cases, stay immunoquiescent (11–13).

NANPs that can respond to temperature, pH changes, light, small molecules, or the presence of oligonucleotides represent an additional level of functional control (19–22) by performing preprogrammed logical operations. For example, the potential therapeutic application of rationally designed RNA logic gates was exemplified by two-stranded RNA switches. These switches were designed to bind an intracellular mRNA (disease marker), initiate conformational changes, and release therapeutically relevant short hairpin RNAs, further activating an RNAi pathway (23). Cell-specific delivery and conditional release of therapeutic cargo was demonstrated by DNA 'nanorobots' activated by simultaneous recognition of key proteins; interactions of aptamers with specific cell-surface receptors dissociated the locking duplexes, exposing the cargo otherwise hidden inside the nanorobot (24). In a similar manner, a DNA robotic device was recently shown to expose a thrombin after interaction with nucleolin on the surface of the tumor vessels *in vivo* (25).

Another strategy for the conditional activation of multiple functionalities is demonstrated by nucleic acid–based assemblies that communicate with each other through sequence complementarity (11,14,15,26–33). The strategy is based on cognate pairs of RNA–DNA hybrids that trigger the activation of different functionalities both *in vitro* and *in vivo*. The central idea is to split the functional entities (e.g. RNA aptamers, a Förster resonance energy transfer (FRET) pair of dyes, DNA templates for *in vitro* transcription, siRNAs, etc.) into two inactive RNA–DNA hybrids. The cognate pair of hybrids is equipped with complementary ssDNA or ssRNA toeholds designed to promote the reassociation of the inactive hybrids via preprogrammed isothermal strand displacements, which restores the intended function. Although up to seven active siRNAs can be released from a single pair of hybrids, the resulting byproduct—long dsDNAs—becomes immunostimulatory (14). We could avoid the formation of long dsDNAs while still maintaining a higher number of split functionalities by embedding up to six hybrids in various RNA and DNA nanoparticles and mixing them with cognate hybrids (15,28,29,31). This technique, however, requires the simultaneous presence of seven assemblies and may be inefficient due to potential problems with intracellular compartmentalization. Recently, we introduced a strategy that relies on interdependent complementary NANPs that require the presence of only one cognate partner for intracellular activation of multiple functionalities (11). However, combining the simple design of conditionally activated NANPs with the maximal capacity for split functionalities, minimal immunotoxicity and removal of byproduct dsDNAs remained a major challenge.

Here, we introduce a simplified and user-friendly approach that allows for conditional activation of RNAi while blocking the transcription of pro-inflammatory genes forming intracellular dsDNAs. Our system is based on a pair of rationally designed RNA–DNA hybrid constructs that, upon mutual recognition in the cytoplasm, give a fluorescent response and release a large number of Dicer substrate (DS) RNAs (34) and short dsDNAs with embedded NF-κB decoys (35–38). NF-κB (nuclear factor kappa-light-chain-enhancer of activated B cells) is expressed in most mammalian cells and remains inactive in the cytoplasm when bound to inhibitory proteins (IκB). There are two classes of NF-κB proteins, and both classes contain the N-terminal DNA-binding domain, which serves as a dimerization interface to other transcription factors as well as the binding site of IκB (39,40). NF-κB can be activated by various stimuli that lead to phosphorylation and subsequent degradation of the IκB, followed by translocation of NF-κB to the nucleus, where it binds to a consensus sequence in the promoter regions of target genes. NF-κB activation can be altered through either IκB overexpression or the introduction of synthetic DNA decoys with a high binding affinity for NF-κB. The NF-κB bound to decoys cannot translocate to the nucleus; consequently, production of pro-inflammatory cytokines becomes limited.

Our system offers multiple advantages, including: (i) very simple design and assembly protocols that significantly lower the production costs and shorten the experimental time; (ii) released dsDNAs that are no longer nonfunctional byproducts, as well as embedded NF-κB decoys that restrain the immunostimulatory responses; (iii) the ability to change the shapes of the hybrids from long fibers to closed polygons by simply changing the orientation of DNA–DNA interacting parts, which in turn leads to distinguished physiochemical and immunological properties. In addition, such a novel strategy increases the control over the precise knockdown of a specific protein and allows the activation of other functionalities, such as FRET, that can be used for real-time intracellular tracking of reassociation.

MATERIALS AND METHODS

All experimental details and sequences used in this work are listed in the Supporting Information.

Design of RNA–DNA fibers and polygons

The schematic explanation of the main design principles used for constructing RNA–DNA fibers and polygons is shown in Figure 1. The correct base pairing was confirmed with NUPACK (41).

Assemblies of hybrid RNA–DNA fibers and polygons and their analysis by native-PAGE

All individual oligonucleotides were purchased from Integrated DNA Technologies, Inc. Fibers and polygons were assembled by combining individual monomers at equimolar concentrations. Assemblies and their reassociations were analyzed on 8% non-denaturing native polyacrylamide (19:1) gel electrophoresis (native-PAGE). A Bio-Rad ChemiDoc MP Imager was used to visualize gels stained with ethidium bromide and view the fluorescence of labeled RNAs. All assemblies were further tested for the presence of bacterial endotoxins by kinetic turbidity limulus amoebocyte lysate (LAL) assay, as detailed in our previous work (42) (Supplementary Table S1).

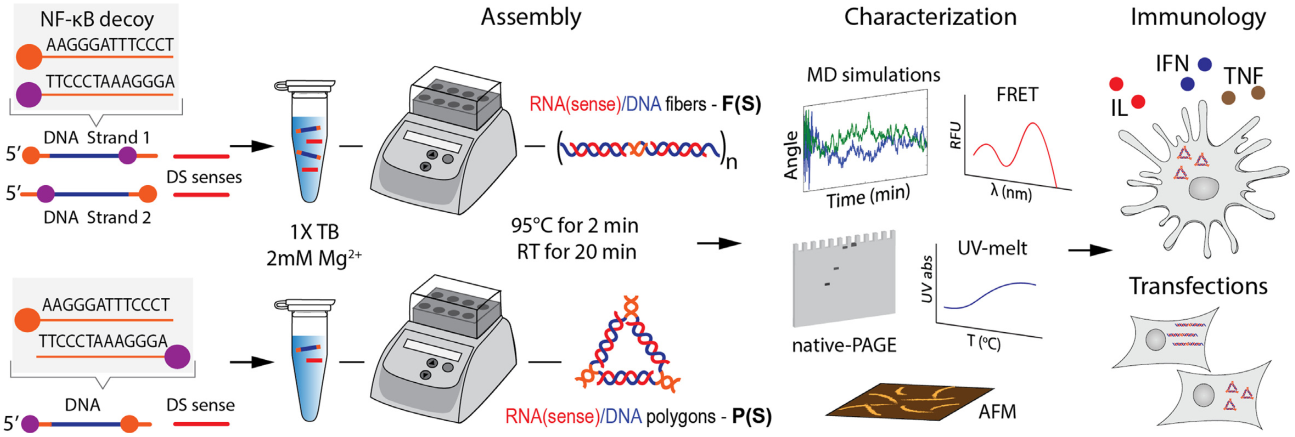

Figure 1. Design principles of RNA–DNA fibers and polygons carring DS RNA sense strands. DNA pieces in blue are reverse complements for DS sense, and pieces in orange are NF-κB decoy–based toeholds (colored balls indicate orientations of the DNA-DNA interactions). Fibers and polygons with antisense strands are designed as their reverse complements.

Ultraviolet melting experiments

Temperature-dependent absorption spectra were recorded at 260 nm on an Agilent spectrophotometer (Agilent, Inc.) equipped with a thermoelectrically controlled cell holder.

Kinetics of reassociation

To determine the kinetics, fluorescently labeled fibers (polygons) were mixed with equimolar cognate partners and aliquoted at set time points. Results were analyzed by native-PAGE using the ChemiDoc MP System.

Blood stability

Fibers (polygons) containing Alexa® 546-labeled RNAs were mixed with 10% (v/v) human blood serum. The mixtures were analyzed by 8% native-PAGE. The bands of treated samples were visualized with the ChemiDoc MP System and analyzed using the complementary Image Lab™ Software.

Atomic force microscopy (AFM) imaging

A freshly cleaved mica surface was modified with APS (1-(3-aminopropyl) silatrane) according to the established protocol (11,12,43) and used for AFM imaging performed on the MultiMode AFM NanoScope IV system (Bruker Instruments, Santa Barbara, CA) in tapping mode. Images were processed by the FemtoScan Online software package (Advanced Technologies Center, Moscow, Russia) (44,45).

Primary human peripheral blood mononuclear cells (PBMCs) and whole-blood culture for analysis of interferon and cytokine secretion

The blood was used within 2 h of collection. Whole-blood cultures were performed to analyze the induction of chemokines and cytokines, while PBMC cultures were used for the analysis of type I interferons. Supernatants were analyzed using a chemiluminescence-based multiplex system (Quansys, Logan, UT, USA). Two independent repeats were prepared for each sample and tested in at least three different donors.

Reporter cell-based assay

HEK-Blue hTLR4 cells (Invivogen, San Diego, CA, USA) were used to assess the functionality of NF-κB decoy oligonucleotides. These cells are engineered to express both human Toll-like receptor (TLR) 4 and, under NF-κB promoter, secreted alkaline phosphatase (SEAP).

Activation of FRET

To determine the reassociation of RNA–DNA assemblies *in vitro*, FRET measurements were performed using a FluoroMax-3 (Jobin Yvon, Horiba). The excitation wavelength was set at 460 nm and the excitation and emission slit widths were set at 5 nm. To track the reassociation of RNA–DNA assemblies in cells, FRET measurements were performed using an LSM 710 confocal microscope (Carl Zeiss) with a 63×, 1.4 NA magnification lens.

Transfection of human breast cancer cells expressing green fluorescent protein (MDA-MB-231/GFP)

MDA-MB-231/GFP cells were used to assay the delivery of functional fibers and polygons. All transfections were performed using Lipofectamine® 2000 (L2K).

Analysis of cell death and cell cycle by propidium iodide staining and flow cytometry

A375 melanoma cells were incubated with transfection complexes prepared in Opti-MEM serum-free medium (Gibco) with Lipofectamine RNAiMAX (Thermo Fisher Scientific) and fibers. Transfected cells were incubated with propidium iodide solution (200 μg/ml RNase A, 0.1% v:v Triton X-100, 20 μg/ml P), and fluorescence was measured by flow cytometry using the Attune NxT cytometer (Life Technologies) to determine the percentage of hypodiploid cells (cell death, subG_1 phase) and the cell cycle (G_0/G_1 and S/G_2/M phases).

Western blot

After the transfection of A375 melanoma cells with fibers, the cells were trypsinized and centrifuged. The cell pellet was dispersed in cell lysis buffer, the homogenate was centrifuged, and the protein content of supernatant was analyzed using primary anti-BRAF antibody (SantaCruz) and peroxidase-conjugated secondary antibody.

Immunofluorescence analysis for detection of NF-κB

Transfected A375 melanoma cells were treated with lipopolysaccharide (LPS); incubated overnight with an anti-NF-κB, p65 subunit (MAB3026, Millipore, 1:100) antibody; then incubated with an Alexa Fluor® 488-conjugated secondary antibody (Molecular Probes, 1:1000) and Hoechst (Sigma-Aldrich, 25 μg/ml). The fluorescence microscope EVOS FL Auto Imaging System (Thermo Fisher Scientific) was used for visualization.

Statistical analysis

All results were presented as mean ± SD of at least three independent experiments. Statistical analyses were performed using one-way analysis of variance (ANOVA) conducted with the GraphPad Prism software. Differences were considered statistically significant with a P-value of <0.05.

RESULTS AND DISCUSSION

Recently, we reported a new concept of interdependent self-recognizing nucleic acid–based NANPs that can conditionally activate multiple functionalities in human cancer cells (11). Here, we offer a new, simplified technology by designing a set of dynamic RNA–DNA fibers and polygons that can interact inside the cells to release a large number of DS RNAs, give a fluorescent response, and activate NF-κB decoys. The design rationale was based on separating DS RNAs and substituting each strand with complementary DNAs. The DNA–NF-κB decoy duplex was also separated, and the individual sequences were added to both ends of complementary DNAs and used as toeholds for assemblies (Figure 1). We found that a simple change in the orientation of one sequence by 180° promotes the formation of either fibers or polygon structures (Figure 2). When complementary hybrid structures are introduced in close proximity inside the cells, the thermodynamically driven isothermal reassociation initiates the release of DS RNAs and NF-κB decoys and activates FRET. The formation of fibers and polygons, along with their further reassociation, was confirmed by native-PAGE and visualized by AFM (Figure 2 and Supplementary Figure S1). The AFM images showed distinct structures of either fibers or polygons, with polygons being present primarily in a triangle shape. Both AFM and native-PAGE confirmed the release of DS RNAs and DNA duplexes when cognate assemblies were incubated together. Aside from the difference in their morphology, fibers and polygons possessed different physicochemical properties and reassociation times (Supplementary Figure S2). A kinetics study showed that polygons reassociated much faster than fibers: polygons required <30 min to complete the reassociation, while fibers required up to 5 h of incubation (Supplementary Figure S2A). Importantly, pre-incubation of individual fibers with Lipofectamnine 2000 (L2K), that would mimic later described transfection experiments, prevented fibers' re-association (Supplementary Figure S2B). These results are consistent with previously reported studies (33,46). The blood stability assays also showed a longer retention time for fibers compared to polygons and both RNA/DNA hybrid constructs being more stable for digestion when compared to RNA (Supplementary Figure S2C).

Absorbance versus temperature profiles were measured to determine the melting transitions of individual polygons and fibers as well as their reassociation products after 5 h of incubation (Supplementary Figure S2D). In polygons P(A) and P(S) and fibers F(A) and F(S), two melting transitions were observed; the first was only a minor melting transition at T_{m1} ~45°C, and the second transition was distinct at T_{m2} ~80°C. Considering the complexity of multi-strand nucleic acid assemblies, our assumption was that T_{m1} is the result of dissociation of the dsDNAs in both fibers and polygons. The T_{m2} then resulted from the dissociation of hybrid RNA–DNA parts of the assemblies. The experimentally measured values were consistent with T_ms measured for corresponding DNA duplex ($T_m \sim 43.4°C$ for 1 μM, 5′-AGGGAAATCCCTT-3′/5′-AAGGGATTTCCCT-3′) and matched the value calculated ($T_{m\ calc} = 43.4°C$) using the Mfold program (47). The UV melting profile for the reassociated complexes exhibited only one strong transition at 80°C that is in agreement with the computed T_ms for the resulting 25-bp RNA duplex ($T_{m\ calc} = 80°C$) and the 53-bp dsDNA ($T_{m\ calc} = 90°C$).

We then computationally analyzed the formation of fibers *in silico*. There were four different and repetitive regions (Figure 3A) that connected the RNA and DNA fragments in the F(S) and the F(A) fibers. These interconnected regions had two distinct conformations. We used iFoldRNA (48) and discrete molecular dynamics (49,50) to reconstruct the tertiary structures of regions 1 and 5, which were the two representative regions of the two conformations. Region 1 had a large gap between the RNA fragment and the DNA fragment, while region 5 resembled a double helix and nearly all the adjacent bases were stacked. We then used Gromacs (51) to perform molecular dynamics for the two regions. The simulation results (Figure 3B) showed that the base pairs near the gap in the F(S) opened rapidly, while the base pairs at the same position in F(A) were maintained during the whole simulation. It suggested that the existence of the gap made the sense fibers more flexible than the antisense fibers. Theoretically, there is the possibility that only one extremely long fiber exists in the solution, which is composed of all the RNA and DNA fragments joined by the regions shown in Figure 3A. The reason why the ideal one single fiber is not maintained is because these connected regions are constantly undergoing thermodynamic changes, which increase the likelihood that some of the connected regions may be broken. Apparently, the average length of fibers in the solution is inversely proportional to the number of connected regions that are broken. Therefore, the more stable the connected regions, the less the connected regions break, and the longer the average length of the fibers. Thus, the fibers assessed by AFM and native-PAGE (Figure

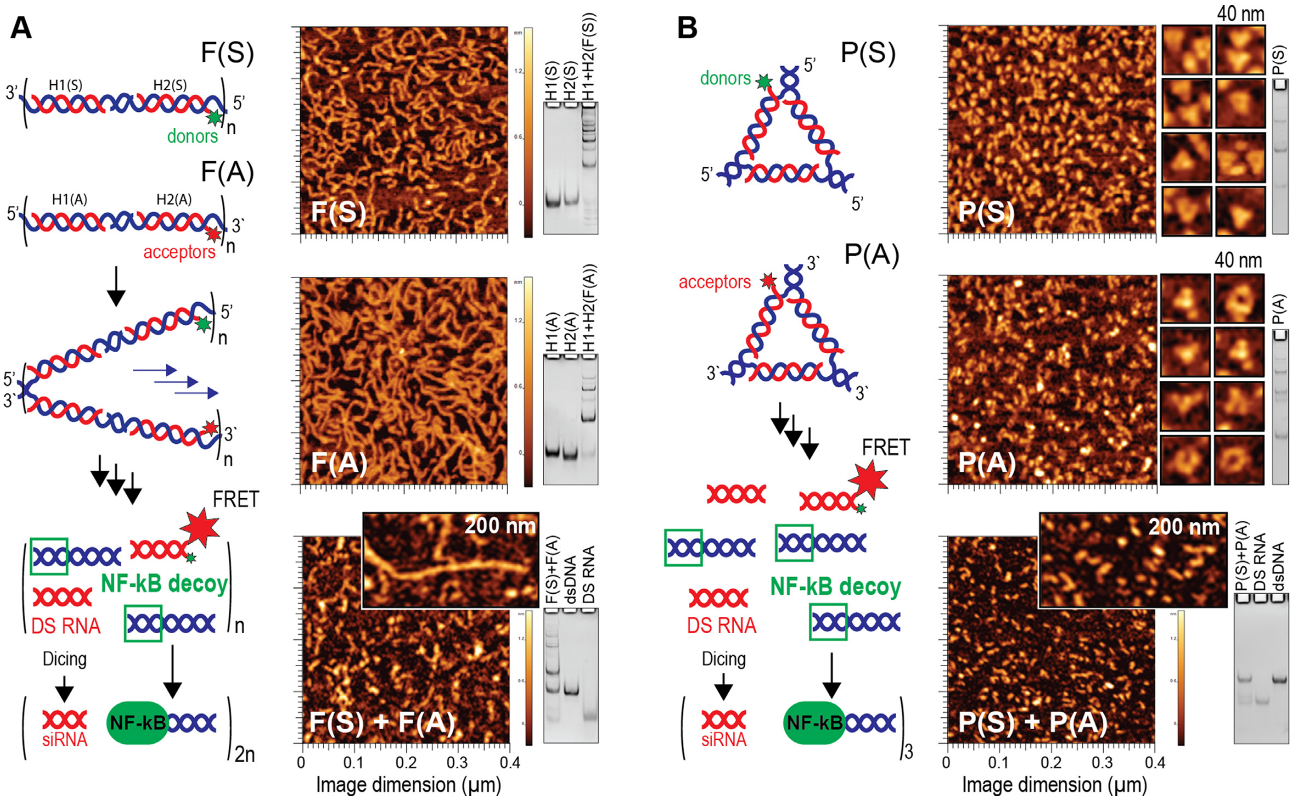

Figure 2. Schematic representation and experimentally verified formation of RNA–DNA hybrid fibers (**A**) and polygons (**B**) and their reassocation that results in release of NF-κB decoys and DS RNAs. NF-κB decoys must fit the groove of NF-kB in order to bind it (77); consequently, the reassociation is needed to release the decoys from the bulky structures of the assemblies. Native-PAGE and AFM confirm the formation of fibers and polygons and their reassociation products.

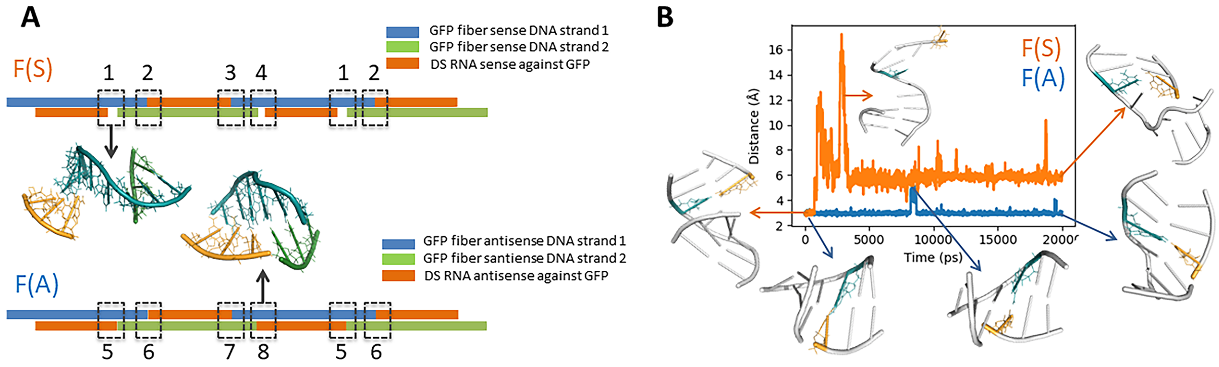

Figure 3. Molecular dynamics simulation of the interconnected region of the sense and antisense fibers. In the fibers, there are four different and repetitive interconnected regions that connect the DNA and RNA fragments. The eight boxes labeled from 1–8 in (**A**) represent the interconnected regions in the sense fibers and the antisense fibers, respectively. Regions 1 and 4 are nearly the same, while regions 2, 3 and 5–8 are the same. Molecular dynamics simulations are performed for regions 1 and 5. Results (**B**) show that the distance between the base pair near the gap in the sense fiber undergoes remarkable changes, while the distance between the base pair near the gap in the antisense fiber is relatively stable during the simulation.

2A and Supplementary Figure S1) showed that the average lengths of F(S) were shorter than F(A) because the higher flexibility made them more easily broken. The opened base pair near the gap would cause more base pairs to open since it gave the fibers higher flexibility. All base pairs in F(S) would finally open, resulting in the formation of more stable helices with F(A). We then utilized the nucleic acid simulation tool (NAST) (52) to perform a coarse-grained molecular dynamics simulation for a triangle and a rectangle, respectively. The results (Supplementary Figure S3) showed that the triangle shape is relatively stable, whereas the rectangle shape was very hard to maintain during the simulation. That explained why triangle shapes are the most common among polygon structures observed by AFM (Figure 2B).

The fibers were programmed to activate multiple split functionalities upon their intracellular activation (FRET, RNAi and formation of functional NF-κB decoys). FRET activation allowed direct visualization of the reassociation process *in vitro* (Figure 4A–B) and in cells (Figure 4C and Supplementary Figure S4), evidencing the differences in the kinetics of the process. To experimentally examine the functionality of released DS RNAs, we transfected human breast cancer cells expressing the enhanced green fluorescent protein (MDA-MB-231/GFP) with cognate fibers and polygons. The GFP can be used as a visual tag for confirming the activation of RNAi, which directly results in the released DS RNAs from the reassociation. The extent of GFP gene silencing was assessed by fluorescence microscopy and flow cytometry (Figure 4D–E and Supplementary Figures S5–S7). Individual sense or antisense fibers and polygons did not alter fluorescence intensity (Supplementary Figures S5–S6). Co-delivery of sense and antisense strands containing fibers (polygons) at different concentrations resulted in a concentration-dependent shift of fluorescence intensity. Interestingly, the co-delivery of individual fibers with cognate ssRNAs resulted in some GFP silencing (Supplementary Figure S7B), thus allowing to specifically activate only an RNAi functionality pre-programmed to fibers. However, due to chemical instability of ssRNA (Supplementary Figure S2C), requirements for a large number of ssRNAs to be present in the same intracellular location with fibers, and inability to activate preprogrammed DNA functionalities, this approach may not be optimal. However, it potentially opens the avenue of research for the delivery of RNA within fiber that will interact with endogenous RNAs (e.g. similar to antimiR oligos (53)).

The reassociation process was also designed to activate decoys designed to bind NF-κB and prevent its translocation to the nucleus upon cell activation. In agreement with previous observations (36), immunofluorescence analysis revealed a perinuclear accumulation of NF-κB upon LPS treatment when the cognate fibers were co-transfected, suggesting that the reassociation of fibers impairs NF-κB nuclear translocation induced by LPS (Figure 4F). To further demonstrate the functional consequences of NF-κB decoy during the intracellular reassociation of fibers (polygons), human PBMCs were treated with constructs (Figure 5 and Supplementary Figure S8). We chose PBMCs as a model system because they are known to be more reliable and predictive of the cytokine storm toxicity than common preclinical animal models such as rodents and nonhuman primates. The significance of this model comes from the tragic experience of a pharmaceutical company (TeGenero Immuno Therapeutics, AG) with a biotechnology product, TGN1412, which resulted in severe toxicity in human patients after successfully passing preclinical safety studies in rats and monkeys; its cytokine storm toxicity was predicted by *in vitro* tests using human PBMCs (54). With PBMC experiments, we used two experimental scenarios for RNA–DNA hybrid complexation with the delivery carrier, L2K, used in all transfections. In the first scenario, fibers and polygons, as well as their complementary structures, were mixed together, then complexed with L2K prior to their addition to the cells (see (F(S)+F(A))-L2K and (P(S)+P(A))-L2K in Figure 5). This scenario guaranteed co-delivery of complementary constructs into the same cell. In the second scenario, fibers and polygons, as well as their complementary structures, were pre-incubated with L2K as two separate samples, after that, these complexes were mixed together for co-delivery (see (F(S)-L2K)+(F(A)-L2K) and (P(S)-L2K+(P(A)-L2K) in Figure 5). This scenario was more challenging to the system than the first scenario because there was no guarantee for the co-delivery into the same cell. For the purpose of this study, we call fibers prepared using these scenarios ‘co-complexed/delivered’ and ‘complexed/co-delivered,’ respectively. Fibers and polygons complexed with L2K and added to cultures as separate samples were used as controls (see F(S)-L2K, F(A)-L2K, P(S)-L2K, and P(A)-L2K in Figure 5). Twenty-four hours after transfection, the PBMCs were challenged with LPS for an additional 24 h. Supernatants were then collected and analyzed for the presence of interleukin-6 (IL-6) and tumor necrosis factor alpha (TNFα). These cytokines are known biomarkers of LPS-mediated activation of PBMCs, and their induction by LPS depends on NF-κB (55). Therefore, if our NF-κB decoy fibers were functional, we would have expected that only the simultaneous presence of fibers and complementary fibers in the same culture would inhibit LPS-induced cytokines. The LPS-only control, representing cells treated with phosphate-buffered saline (PBS) for the first 24 h and LPS alone for the second 24 h, demonstrated that PBMCs still functioned and produced both cytokines in response to LPS after 48 h of total cell culture (compare PBS and PBS/LPS samples in Figure 5B and C). When complementary fibers were delivered separately prior to LPS stimulation, no inhibition in the LPS-induced IL-6 and TNFα was observed. A higher level of both cytokines was noticed and was consistent with the known phenomenon of an increase in the LPS-mediated inflammation by certain types of nanomaterials (compare samples F(S)-L2K and F(A)-L2K to LPS-only in Figure 5B–C) (56–59). In contrast, co-complexed/delivered and complexed/co-delivered fibers resulted in the inhibition of LPS-induced IL-6 and TNFα (compare samples (F(S)+F(A))-L2K and (F(S)-L2K)+(F(A)-L2K) to individual fibers and LPS-only control). These data were consistent with the expected inhibition of NF-κB due to the formation of an NF-κB decoy functional oligonucleotide system following the delivery of both components into the cell. The complete inhibition could not be achieved, likely due to the remaining effect of co-treatment between the LPS and the fibers. There was no statistically significant difference between co-complexed/delivered and complexed/co-delivered fibers, although the decrease in cytokine production observed with co-complexed/co-delivered fibers was more pronounced ((F(S)+F(FA))-L2K versus (F(S)-L2K)+(F(A)-L2K) in Figure 5B and C). Altogether these data demonstrate the robustness of the system and suggest that co-delivery can be considered to further ensure the efficiency of the system across cells from different individuals and various types. The same trends were observed in polygons (compare P(S)-L2K and P(A)-L2K as single treatments to (P(S)+P(A))-L2K and (P(S)-L2K)+(P(A)-L2K) in Figure 5B and C).

Human PBMCs were a complex system because they contained multiple cell types that expressed various receptors and transcription factors contributing differently to the LPS-triggered inflammatory response. Moreover, there are several factors such as (i) known polymorphisms of genes

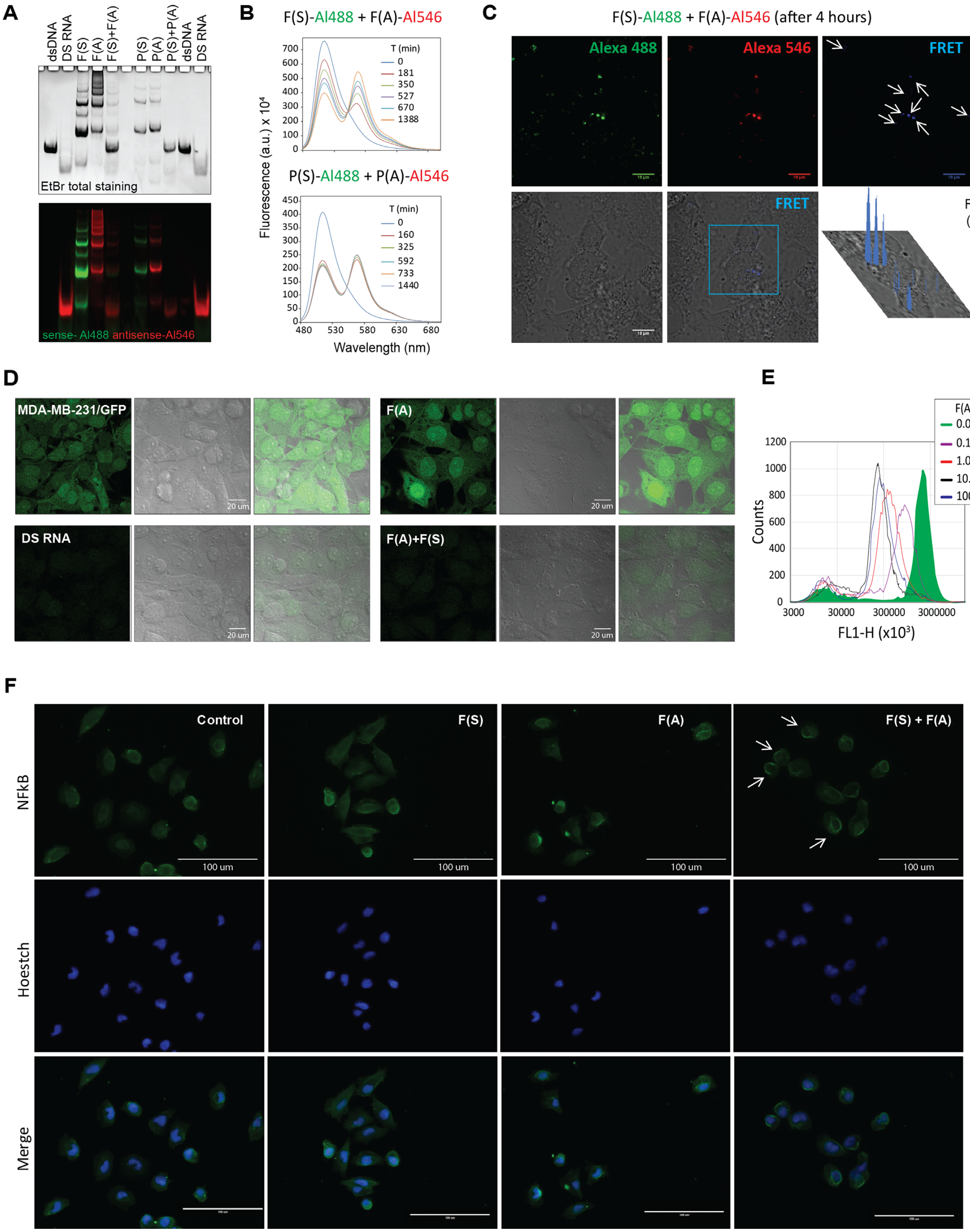

Figure 4. Intracellular reassociation of fibers followed with FRET, gene silencing, and perinuclear NF-κB accumulation upon LPS treatment. (**A**, **B**) Re-association of fluorescently labeled fibers and polygons confirmed by native-PAGE and FRET measurements. (**C**) FRET (indicated with arrows) observed upon reassociation of fibers in human breast cancer cells (MDA-MB-231). (**D**, **E**) Reassociation of fibers promotes the release of DS RNAs specifically designed to target GFP. Three days after the transfection of cells (MDA-MB-231/GFP), GFP silencing was confirmed by fluorescence microscopy and flow cytometry. (**F**) Cells transfected with fibers were treated with LPS for 4 h. After fixation and permeabilization, cells were processed for immunofluorescence staining with NF-κB (p65) using Alexa Fluor 488-conjugated secondary antibodies (green) and Hoechst (blue). Panel F(S) + F(A) reveals perinuclear accumulation of NF-κB (arrows), suggesting that reassociated fibers impair NF-κB nuclear translocation induced by LPS (scale bar: 100 μm).

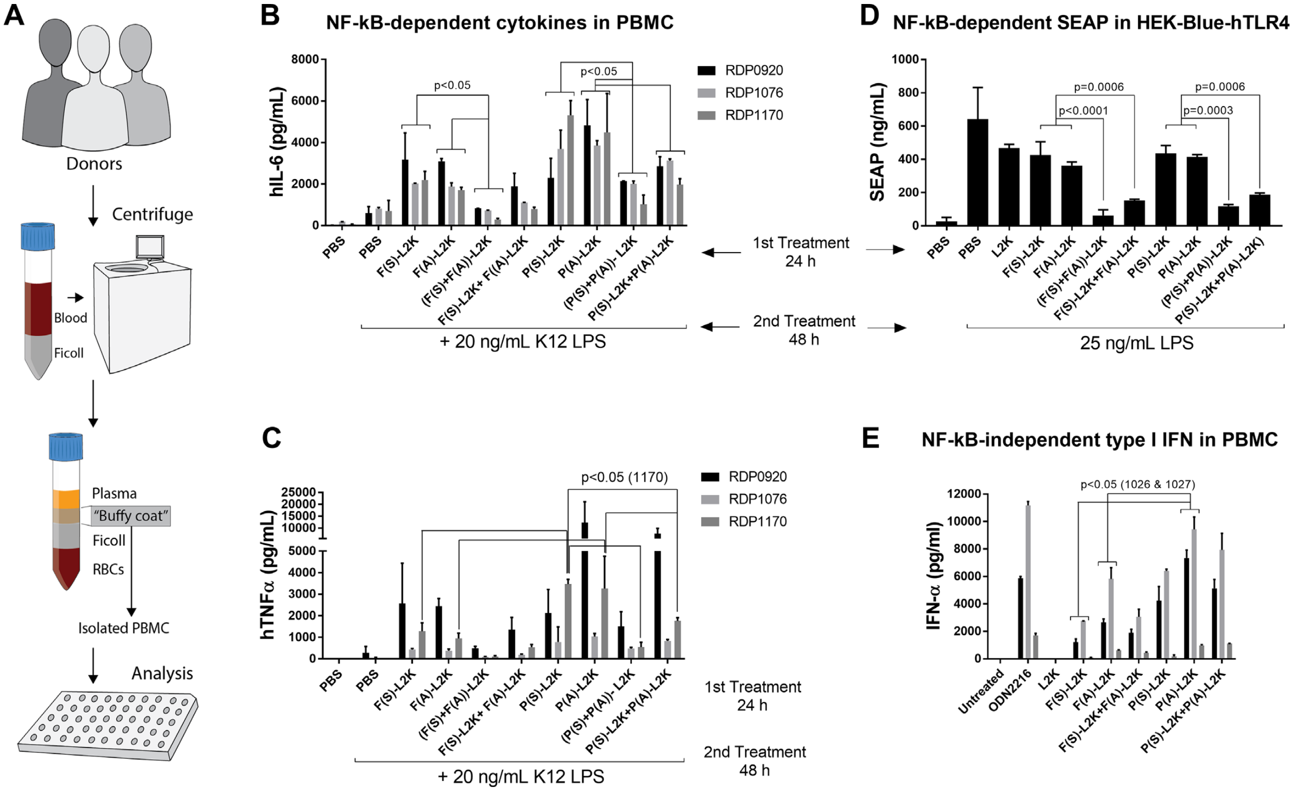

Figure 5. Functional effects of RNA–DNA fibers on NF-κB-dependent and -independent expression of pro-inflammatory markers. Human peripheral blood mononuclear cells from at least three donor volunteers and the reporter cell line HEK-Blue hTLR4 were studied. (**A**) Schematics explaining PBMC isolation and further analysis. (**B**, **C**) PBMCs were treated for the first 24 h with controls or fibers and then stimulated with 20 ng/mL of ultrapure bacterial K12 LPS. Levels of IL-6 (B) and TNFα (C) were measured in the supernatants by multiplex ELISA. (**D**) Reporter cell line HEK-Blue hTLR4 was transfected with fibers and, 24 h later, stimulated with ultrapure K12 LPS. The cells were incubated for an additional 24 h, and the levels of NF-κB-dependent SEAP were measured in supernatants. (**E**) PBMCs were treated with positive control (ODN2216), negative control (L2K alone), or fibers for 24 h, and the levels of type I interferon (IFNα) were assessed by multiplex ELISA. PBS: phospate-buffered saline; L2K: Lipofectamine 2000; LPS: *E. coli* K12 lipopolysacharide; ODN2216: CpG oligonucleotide known to induce IFNα.

encoding proteins involved in the LPS response; (ii) the induction of IFN by fibers, which, among other mechanisms, may contribute to the greater induction of the pro-inflammatory cytokines by the LPS and (iii) challenges with the delivery of nucleic acid nanoparticles into primary cell cultures in vitro, which collectively may complicate the verification of NF-κB specificity in the primary cultures of blood cells from individual human donors. Therefore, to further verify the specificity of the response to NF-κB, we conducted a follow-up study using the reporter cell line HEK-Blue hTLR4. These cells express SEAP under the NF-κB promoter, which can be activated only through one pathway that is triggered by bacterial LPS. When RNA–DNA fibers were co-transfected, and the cells were stimulated with LPS, the NF-κB-dependent SEAP production was inhibited regardless of the scenario used for fiber complexation with L2K (Figure 5D, compare (F(S)+F(A))-L2K and (F(S)-L2K)+(F(A)-L2K) to PBS/LPS and L2K/LPS controls). The same trend was observed in polygons (Figure 5D, compare (P(S)+P(A))-L2K and (P(S)-L2K)+(P(A)-L2K) to PBS/LPS and L2K/LPS controls). These findings are consistent with the intended mechanism of action. When only individual fibers or polygons were delivered to the cells, no such inhibition was observed, further confirming the specificity of the mechanism of action to NF-κB (Figure 5D, compare F(S)-L2K, F(A)-L2K, P(S)-L2K, and P(A)-L2K to PBS/LPS and L2K/LPS controls). These data confirmed that fibers' and polygons' reassociation is specific to NF-κB decoy formation.

The induction of pro-inflammatory cytokines and interferons (IFNs) in human immune cells is a tool commonly used for vaccines and immunotherapies when activation of the immune system is desirable (60). However, excessive production of the cytokines, particularly TNFα, may cause tissue necrosis at the site of injection (61). Decreasing the injection site reactions in patients is therefore considered an essential safety goal for vaccines and immunotherapies (62–65). TLR agonists are commonly used as adjuvants for their ability to induce cytokines and interferons (66). Some current approaches for immune system stimulation include using nanoparticles to deliver a TLR ligand or combining different TLR agonists to achieve both cytokine and interferon induction (67,68). For example, TLR4 adjuvants, which are more potent at inducing cytokines, can be combined with TLR9 adjuvants, which are more potent at inducing interferons (66). In the traditional approach, such a combination is associated with a higher risk of injection-site reactions in sensitive individu-

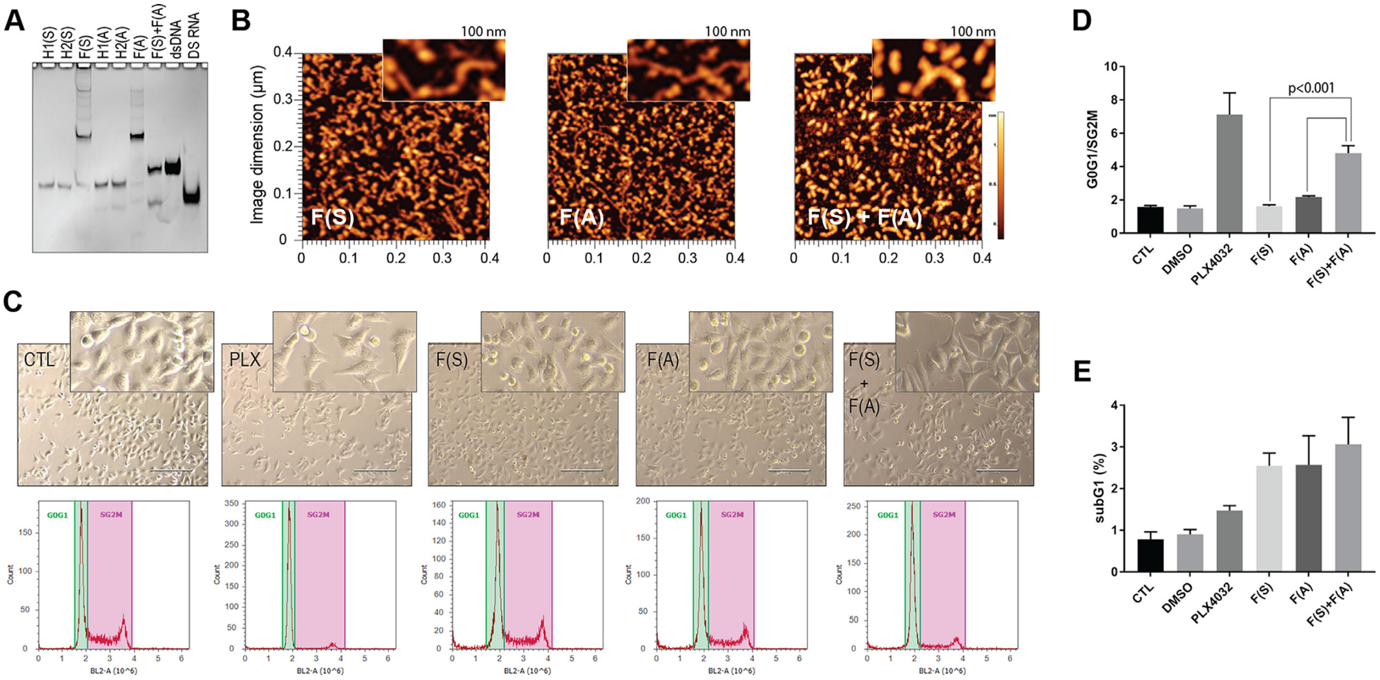

Figure 6. Growth-inhibition effects and morphological alterations upon complementary intracellular reassociation of fibers. (**A**) Native-PAGE shows the formation of sense F(S) and antisense F(A) fibers and their reassociation products F(S) + F(A). (**B**) AFM images of F(S), F(A), and the reassociated F(S) + F(A) that release NF-κB decoys and DS RNAs. A375 melanoma cells were transfected with nanofibers and stained with the fluorescent intercalating agent propidium iodide 48 h post-transfection. Flow cytometry analysis was performed to evaluate cell viability and DNA content in the cell cycle. (**C**) *Upper panel:* Pictures taken at 48 h post-transfection show melanoma cells' morphological changes to a fusiform phenotype upon intracellular association of fibers, similar to cells under treatment with PLX4032 (magnification: 20×, scale bar: 200 µm). *Lower panel:* Histograms representing the number of cells in G_0/G_1 (quiescence/checkpoint 1) and $S/G_2/M$ (checkpoint 2/mitosis) phases of the cell cycle. (**D**) Analysis of cell cycle arrest, characterized by the ratio of G_0/G_1 over $S/G_2/M$, showing significant accumulation of cells in G_0/G_1 phases when fibers were associated F(S) + F(A). (**E**) Analysis of cell death, observed by the accumulation of haplodiploid cells in the subG_1 phase, indicating the process of nuclear DNA fragmentation. CTL –control cells without treatment; PLX: PLX4032 (vemurafenib).

als. Therefore, we hypothesized that the fibers and polygons described in our study could provide a desirable tool for vaccine and immunotherapy adjuvant production by regulating the amounts of pro-inflammatory cytokines triggered by NF-κB-dependent TLR4 co-adjuvants while inducing interferons via an NF-κB-independent mechanism. To verify that designed fibers and polygons are capable of inducing type I IFNs and that such induction is not affected by the NF-κB decoy function, we tested supernatants collected from PBMC cultures for the presence of type I interferons. We confirmed that fibers and polygons stimulate interferons and that this property is not affected when sense and antisense fibers or polygons are combined to inhibit NF-κB (Figure 5E). An inter-donor variability in IFN response was observed, in that a stronger IFN induction was detected in cultures of one out of three donors in response to the antisense fiber (Figure 5E and Supplementary Figure S8). This variability as well as a difference in the potency of IFN induction between fibers and polygons are consistent with the current knowledge of the IFN induction by RNA nanoparticles in primary human cells (69). While the scope of our project did not include establishing the relation of this property to a decrease in injection-site reactions in humans, the data presented in this study are very promising and warrant further, more focused investigation. Interestingly enough, polygons were more potent inducers of type I IFNs in some donors (Figure 5E and Supplementary Figure S8), suggesting that the shape of the assemblies was an important prerequisite to their adjuvanticity.

To show the therapeutic potential of this multipronged approach, we treated human melanoma cell line with RNA–DNA fibers designed to release the NF-κB decoy along with DS RNAs targeting the mutated *BRAF* gene (70–72) (Figure 6). Melanoma is a form of skin cancer with poor prognosis, and because conventional therapies are consistently ineffective and the disease often recurs, melanomas are one of the prime candidates for the development of novel combinatorial treatment strategies. The discovery that missense mutations in the *BRAF* gene were present in approximately 60% of melanomas encouraged the development of RAF inhibitors to block the constitutive activation of this gene, an essential regulator of MAPK cell proliferation and survival pathways. In 2011, the U.S. Food and Drug Administration approved vemurafenib for the treatment of metastatic melanomas harboring the $BRAF^{V600E}$ mutation. Despite the high response rates of patients to vemurafenib, relapse still occurs within months of initiating the treatment in most cases (73). Activation of the NF-κB pathway is among the multiple mechanisms of acquired resistance to vemurafenib in melanomas, and the inhibition of this transcription factor increases cell death of vemurafenib-resistant cells (74,75). In this scenario, melanoma cells represent an attractive model to evaluate the therapeutic potential of fibers designed to release DS RNAs targeting mutated *BRAF* and DS DNA as an NF-κB decoy. We treated A375 melanoma cells, which carry the *BRAF*^{V600E} mutation, with fibers F(S), F(A) and F(S)+F(A) (Figure 6D and Supplementary Figure S10). Cell cycle analysis by propidium iodide intercalation revealed that, after association, the fibers induced an accumulation of cells in the G_0G_1 phase, similar to the cells treated with vemurafenib (PLX4032) (Figure 6D). Histograms illustrating the distribution of melanoma cells throughout the cell cycle (G_0/G_1 and $S/G_2/M$) (Figure 6E) showed a similar cell cycle arrest profile between associated nanofibers and PLX4032. Therefore, the cytostatic effect observed in melanoma cells upon treatment with fibers was similar to the effects of treatment with PLX4032. Fibers also induced cell-shape alterations similar to PLX4032, as observed by the presence of fusiform cells among epithelial cells after treatment, which was more evident with F-actin staining and the apparent microtubule polarization for the maintenance of NF-κB in an inactive state (76) (Supplementary Figure S9). These data suggested that the DS RNAs released by nanofibers to target the mutated *BRAF* gene in melanoma cells resulted in a similar cellular response as observed with PLX4032. A drawback of the PLX4032 treatment is the emergence of a resistance mechanism through the activation of the NF-κB pathway, as displayed by the A375 melanoma cells. Beyond the silencing of mutated *BRAF*, reassociation of the fibers releases an NF-κB decoy that induces the retention of NF-κB in the cytoplasm of the cells, which could thereby revert the resistance mechanism. These results suggest the promising use of RNA–DNA nanofibers as a strategy to overcome the resistance of melanoma cells to PLX4032 treatment. Combinatorial approaches are emerging as being critical for successful therapies, and the development of smart nanoparticles capable of releasing multiple functionalities in a controlled fashion can represent a significant advantage in that direction.

In conclusion, the responsive behaviors of this novel system are determined by the specific design principles of individual constructs, the type of their assembly, and physicochemical properties. The innovative use of dynamic systems presents multiple advantages: (i) fibers and polygons can be programmed to gather multiple different functionalities for their simultaneous delivery to cells, thus allowing simultaneous targeting of various biological pathways with higher synergistic effects; (ii) the relatively inexpensive cost of the materials and simple assembly protocols of fibers and polygons enable their economic industrial-scale production; (iii) thermal and chemical stabilities of constructs can be fine-tuned, and other functionalities can be programmed into constructs (e.g. fluorophores) to induce multi-responsive behavior; (iv) naked constructs avoid non-specific cell penetration due to their negative charge and (v) the immunological properties of fibers and polygons are tunable and can potentially be predicted.

This work expands our understanding of different parameters in design principles and formulation protocols of RNA–DNA nanoassemblies, and it allows us to identify the best settings and techniques for possible pipeline production of dynamic, functionally interdependent systems that can be used for a broad spectrum of biological applications.

SUPPLEMENTARY DATA

Supplementary Data are available at NAR Online.

ACKNOWLEDGEMENTS

The authors would like to thank Alexander Lushnikov and Alexey Krasnoslobodtsev for performing AFM imaging at the Nanoimaging Core Facility at the University of Nebraska Medical Center.

FUNDING

Research reported in this publication was supported by the National Institute Of General Medical Sciences of the National Institutes of Health under Award Number R01GM120487 (to K.A.A). The content is solely the responsibility of the authors and does not necessarily represent the official views of the National Institutes of Health. M.R. was supported in part by funding provided by NSF-REU and DOD-ASSURE under NSF Grant No. CHE 1460867 and NanoSURE REU under NSF Grant No. DMR 1757619. This project has been funded in whole or in part with Federal funds from the National Cancer Institute, National Institutes of Health, under contract HHSN261200800001E (E.H., M.A.D., and M.V.). N.V.D. also acknowledges support from NIH grants R01-GM114015, R01-GM064803, and R01-GM123247. The content of this publication does not necessarily reflect the views or policies of the Department of Health and Human Services, nor does mention of trade names, commercial products or organizations imply endorsement by the US Government. This research was also supported in part by a FAPESP-USP SPRINT grant from The Graduate School at the University of North Carolina at Charlotte (to K.A.A.) and São Paulo Research Foundation (FAPESP) under FAPESP Grants No. 2015/22814-5 (to R.C.) and 2017/50029-6 (SPRINT to R.C).

Conflict of interest statement. None declared.

REFERENCES

1. Vogel,A.B., Lambert,L., Kinnear,E., Busse,D., Erbar,S., Reuter,K.C., Wicke,L., Perkovic,M., Beissert,T., Haas,H. *et al.* (2018) Self-Amplifying RNA vaccines give equivalent protection against influenza to mRNA vaccines but at much lower doses. *Mol. Ther.*, **26**, 446–455.
2. Chakraborty,C., Sharma,A.R., Sharma,G., Doss,C.G.P. and Lee,S.S. (2017) Therapeutic miRNA and siRNA: Moving from bench to clinic as next generation medicine. *Mol. Ther. Nucleic Acids*, **8**, 132–143.
3. Sun,H. and Zu,Y. (2015) Aptamers and their applications in nanomedicine. *Small*, **11**, 2352–2364.
4. Adams,D., Gonzalez-Duarte,A., O'Riordan,W.D., Yang,C.C., Ueda,M., Kristen,A.V., Tournev,I., Schmidt,H.H., Coelho,T., Berk,J.L. *et al.* (2018) Patisiran, an RNAi therapeutic, for hereditary transthyretin amyloidosis. *N. Engl. J. Med.*, **379**, 11–21.
5. Grijalvo,S., Alagia,A., Jorge,A.F. and Eritja,R. (2018) Covalent strategies for targeting messenger and Non-Coding RNAs: An updated review on siRNA, miRNA and antimiR conjugates. *Genes (Basel)*, **9**, E74.
6. Sasaki,S. and Guo,S. (2018) Nucleic acid therapies for cystic fibrosis. *Nucleic Acid Ther.*, **28**, 1–9.
7. Nimjee,S.M., White,R.R., Becker,R.C. and Sullenger,B.A. (2017) Aptamers as therapeutics. *Annu. Rev. Pharmacol. Toxicol.*, **57**, 61–79.
8. Barbalat,R., Ewald,S.E., Mouchess,M.L. and Barton,G.M. (2011) Nucleic acid recognition by the innate immune system. *Annu. Rev. Immunol.*, **29**, 185–214.

9. Junt,T. and Barchet,W. (2015) Translating nucleic acid-sensing pathways into therapies. *Nat. Rev. Immunol.*, **15**, 529–544.
10. Radovic-Moreno,A.F., Chernyak,N., Mader,C.C., Nallagatla,S., Kang,R.S., Hao,L., Walker,D.A., Halo,T.L., Merkel,T.J., Rische,C.H. *et al.* (2015) Immunomodulatory spherical nucleic acids. *Proc. Natl. Acad. Sci. U.S.A.*, **112**, 3892–3897.
11. Halman,J.R., Satterwhite,E., Roark,B., Chandler,M., Viard,M., Ivanina,A., Bindewald,E., Kasprzak,W.K., Panigaj,M., Bui,M.N. *et al.* (2017) Functionally-interdependent shape-switching nanoparticles with controllable properties. *Nucleic Acids Res.*, **45**, 2210–2220.
12. Johnson,M.B., Halman,J.R., Satterwhite,E., Zakharov,A.V., Bui,M.N., Benkato,K., Goldsworthy,V., Kim,T., Hong,E., Dobrovolskaia,M.A. *et al.* (2017) Programmable Nucleic Acid Based polygons with controlled neuroimmunomodulatory properties for predictive QSAR modeling. *Small*, **13**, doi:10.1002/smll.201701255.
13. Bui,M.N., Brittany Johnson,M., Viard,M., Satterwhite,E., Martins,A.N., Li,Z, Marriott,I., Afonin,K.A. and Khisamutdinov,E.F. (2017) Versatile RNA tetra-U helix linking motif as a toolkit for nucleic acid nanotechnology. *Nanomedicine*, **13**, 1137–1146.
14. Afonin,K.A., Desai,R., Viard,M., Kireeva,M.L., Bindewald,E., Case,C.L., Maciag,A.E., Kasprzak,W.K., Kim,T., Sappe,A. *et al.* (2014) Co-transcriptional production of RNA-DNA hybrids for simultaneous release of multiple split functionalities. *Nucleic Acids Res.*, **42**, 2085–2097.
15. Afonin,K.A., Viard,M., Kagiampakis,I., Case,C.L., Dobrovolskaia,M.A., Hofmann,J., Vrzak,A., Kireeva,M., Kasprzak,W.K., KewalRamani,V.N. *et al.* (2015) Triggering of RNA interference with RNA-RNA, RNA-DNA, and DNA-RNA nanoparticles. *ACS Nano*, **9**, 251–259.
16. Khisamutdinov,E.F., Li,H., Jasinski,D.L., Chen,J., Fu,J. and Guo,P. (2014) Enhancing immunomodulation on innate immunity by shape transition among RNA triangle, square and pentagon nanovehicles. *Nucleic Acids Res.*, **42**, 9996–10004.
17. Li,H., Lee,T., Dziubla,T., Pi,F., Guo,S., Xu,J., Li,C., Haque,F., Liang,X.J. and Guo,P. (2015) RNA as a stable polymer to build controllable and defined nanostructures for material and biomedical applications. *Nano Today*, **10**, 631–655.
18. Khisamutdinov,E.F., Jasinski,D.L. and Guo,P. (2014) RNA as a boiling-resistant anionic polymer material to build robust structures with defined shape and stoichiometry. *ACS Nano*, **8**, 4771–4781.
19. Saragliadis,A., Krajewski,S.S., Rehm,C., Narberhaus,F. and Hartig,J.S. (2013) Thermozymes: Synthetic RNA thermometers based on ribozyme activity. *RNA Biol.*, **10**, 1010–1016.
20. Modi,S., Nizak,C., Surana,S., Halder,S. and Krishnan,Y. (2013) Two DNA nanomachines map pH changes along intersecting endocytic pathways inside the same cell. *Nat. Nanotechnol.*, **8**, 459–467.
21. Morse,D.P., Nevins,C.E., Aggrey-Fynn,J., Bravo,R.J., Pfaeffle,H.O.I. and Laney,J.E. (2018) Sensitive and specific detection of ligands using engineered riboswitches. *J. Biotechnol.*, **272–273**, 22–32.
22. Andersen,E.S., Dong,M., Nielsen,M.M., Jahn,K., Subramani,R., Mamdouh,W., Golas,M.M., Sander,B., Stark,H., Oliveira,C.L. *et al.* (2009) Self-assembly of a nanoscale DNA box with a controllable lid. *Nature*, **459**, 73–76.
23. Bindewald,E., Afonin,K.A., Viard,M., Zakrevsky,P., Kim,T. and Shapiro,B.A. (2016) Multistrand structure prediction of Nucleic Acid Assemblies and design of RNA switches. *Nano Lett.*, **16**, 1726–1735.
24. Douglas,S.M., Bachelet,I. and Church,G.M. (2012) A logic-gated nanorobot for targeted transport of molecular payloads. *Science*, **335**, 831–834.
25. Li,S., Jiang,Q., Liu,S., Zhang,Y., Tian,Y., Song,C., Wang,J., Zou,Y., Anderson,G.J., Han,J.Y. *et al.* (2018) A DNA nanorobot functions as a cancer therapeutic in response to a molecular trigger in vivo. *Nat. Biotechnol.*, **36**, 258–264.
26. Afonin,K.A., Viard,M., Martins,A.N., Lockett,S.J., Maciag,A.E., Freed,E.O., Heldman,E., Jaeger,L., Blumenthal,R. and Shapiro,B.A. (2013) Activation of different split functionalities on re-association of RNA-DNA hybrids. *Nat. Nanotechnol.*, **8**, 296–304.
27. Afonin,K.A., Kasprzak,W.K., Bindewald,E., Kireeva,M., Viard,M., Kashlev,M. and Shapiro,B.A. (2014) In silico design and enzymatic synthesis of functional RNA nanoparticles. *Acc. Chem. Res.*, **47**, 1731–1741.
28. Afonin,K.A., Viard,M., Koyfman,A.Y., Martins,A.N., Kasprzak,W.K., Panigaj,M., Desai,R., Santhanam,A., Grabow,W.W., Jaeger,L. *et al.* (2014) Multifunctional RNA nanoparticles. *Nano Lett.*, **14**, 5662–5671.
29. Dao,B.N., Viard,M., Martins,A.N., Kasprzak,W.K., Shapiro,B.A. and Afonin,K.A. (2015) Triggering RNAi with multifunctional RNA nanoparticles and their delivery. *DNA RNA Nanotechnol.*, **1**, 27–38.
30. Martins,A.N., Ke,W., Jawahar,V., Striplin,M., Striplin,C., Freed,E.O. and Afonin,K.A. (2017) Intracellular reassociation of RNA-DNA hybrids that activates RNAi in HIV-Infected cells. *Methods Mol. Biol.*, **1632**, 269–283.
31. Afonin,K.A., Viard,M., Tedbury,P., Bindewald,E., Parlea,L., Howington,M., Valdman,M., Johns-Boehme,A., Brainerd,C., Freed,E.O. *et al.* (2016) The use of minimal RNA toeholds to trigger the activation of multiple functionalities. *Nano Lett.*, **16**, 1746–1753.
32. Rogers,T.A., Andrews,G.E., Jaeger,L. and Grabow,W.W. (2015) Fluorescent monitoring of RNA assembly and processing using the split-spinach aptamer. *ACS Synth. Biol.*, **4**, 162–166.
33. Groves,B., Chen,Y.J., Zurla,C., Pochekailov,S., Kirschman,J.L., Santangelo,P.J. and Seelig,G. (2016) Computing in mammalian cells with nucleic acid strand exchange. *Nat. Nanotechnol.*, **11**, 287–294.
34. Rose,S.D., Kim,D.H., Amarzguioui,M., Heidel,J.D., Collingwood,M.A., Davis,M.E., Rossi,J.J. and Behlke,M.A. (2005) Functional polarity is introduced by Dicer processing of short substrate RNAs. *Nucleic Acids Res.*, **33**, 4140–4156.
35. Mitchell,S., Vargas,J. and Hoffmann,A. (2016) Signaling via the NFκB system. *Wiley Interdiscip. Rev. Syst. Biol. Med.*, **8**, 227–241.
36. Porciani,D., Tedeschi,L., Marchetti,L., Citti,L., Piazza,V., Beltram,F. and Signore,G. (2015) Aptamer-Mediated codelivery of doxorubicin and NF-kappaB decoy enhances chemosensitivity of pancreatic tumor cells. *Mol. Ther. Nucleic Acids*, **4**, e235.
37. Griesenbach,U., Scheid,P., Hillery,E., de Martin,R., Huang,L., Geddes,D.M. and Alton,E.W. (2000) Anti-inflammatory gene therapy directed at the airway epithelium. *Gene Ther.*, **7**, 306–313.
38. Kim,K.H., Lee,E.S., Cha,S.H., Park,J.H., Park,J.S., Chang,Y.C. and Park,K.K. (2009) Transcriptional regulation of NF-kappaB by ring type decoy oligodeoxynucleotide in an animal model of nephropathy. *Exp. Mol. Pathol.*, **86**, 114–120.
39. Brasier,A.R. (2006) The NF-kappaB regulatory network. *Cardiovasc. Toxicol.*, **6**, 111–130.
40. Gilmore,T.D. (2006) Introduction to NF-kappaB: players, pathways, perspectives. *Oncogene*, **25**, 6680–6684.
41. Zadeh,J.N., Steenberg,C.D., Bois,J.S., Wolfe,B.R., Pierce,M.B., Khan,A.R., Dirks,R.M. and Pierce,N.A. (2011) NUPACK: Analysis and design of nucleic acid systems. *J. Comput. Chem.*, **32**, 170–173.
42. Afonin,K.A., Grabow,W.W., Walker,F.M., Bindewald,E., Dobrovolskaia,M.A., Shapiro,B.A. and Jaeger,L. (2011) Design and self-assembly of siRNA-functionalized RNA nanoparticles for use in automated nanomedicine. *Nat. Protoc.*, **6**, 2022–2034.
43. Alibakhshi,M.A., Halman,J.R., Wilson,J., Aksimentiev,A., Afonin,K.A. and Wanunu,M. (2017) Picomolar fingerprinting of nucleic acid nanoparticles using solid-state nanopores. *ACS Nano*, **11**, 9701–9710.
44. Shlyakhtenko,L.S., Gall,A.A. and Lyubchenko,Y.L. (2013) Mica functionalization for imaging of DNA and protein-DNA complexes with atomic force microscopy. *Methods Mol. Biol.*, **931**, 295–312.
45. Shlyakhtenko,L.S., Gall,A.A., Filonov,A., Cerovac,Z., Lushnikov,A. and Lyubchenko,Y.L. (2003) Silatrane-based surface chemistry for immobilization of DNA, protein-DNA complexes and other biological materials. *Ultramicroscopy*, **97**, 279–287.
46. Afonin,K.A., Viard,M., Martins,A.N., Lockett,S.J., Maciag,A.E., Freed,E.O., Heldman,E., Jaeger,L., Blumenthal,R. and Shapiro,B.A. (2013) Activation of different split functionalities upon re-association of RNA-DNA hybrids. *Nat. Nanotechnol.*, **8**, 296–304.
47. Markham,N.R. and Zuker,M. (2005) DINAMelt web server for nucleic acid melting prediction. *Nucleic Acids Res.*, **33**, W577–W581.
48. Sharma,S., Ding,F. and Dokholyan,N.V. (2008) iFoldRNA: three-dimensional RNA structure prediction and folding. *Bioinformatics*, **24**, 1951–1952.
49. Shirvanyants,D., Ding,F., Tsao,D., Ramachandran,S. and Dokholyan,N.V. (2012) Discrete molecular dynamics: an efficient and versatile simulation method for fine protein characterization. *J. Phys. Chem. B*, **116**, 8375–8382.

50. Ding,F., Sharma,S., Chalasani,P., Demidov,V.V., Broude,N.E. and Dokholyan,N.V. (2008) Ab initio RNA folding by discrete molecular dynamics: from structure prediction to folding mechanisms. *RNA*, **14**, 1164–1173.
51. Berendsen,H.J.C., van der Spoel,D. and van Drunen,R. (1995) GROMACS: a message-passing parallel molecular dynamics implementation. *Comput. Phys. Commun.*, **91**, 43–56.
52. Jonikas,M.A., Radmer,R.J., Laederach,A., Das,R., Pearlman,S., Herschlag,D. and Altman,R.B. (2009) Coarse-grained modeling of large RNA molecules with knowledge-based potentials and structural filters. *RNA*, **15**, 189–199.
53. Stenvang,J., Petri,A., Lindow,M., Obad,S. and Kauppinen,S. (2012) Inhibition of microRNA function by antimiR oligonucleotides. *Silence*, **3**, 1.
54. Vessillier,S., Eastwood,D., Fox,B., Sathish,J., Sethu,S., Dougall,T., Thorpe,S.J., Thorpe,R. and Stebbings,R. (2015) Cytokine release assays for the prediction of therapeutic mAb safety in first-in man trials–Whole blood cytokine release assays are poorly predictive for TGN1412 cytokine storm. *J. Immunol. Methods*, **424**, 43–52.
55. Zuckerman,S.H., Evans,G.F. and Guthrie,L. (1991) Transcriptional and post-transcriptional mechanisms involved in the differential expression of LPS-induced IL-1 and TNF mRNA. *Immunology*, **73**, 460–465.
56. Dobrovolskaia,M.A. (2015) Pre-clinical immunotoxicity studies of nanotechnology-formulated drugs: challenges, considerations and strategy. *J. Control. Release*, **220**, 571–583.
57. Inoue,K. (2011) Promoting effects of nanoparticles/materials on sensitive lung inflammatory diseases. *Environ. Health Prev. Med.*, **16**, 139–143.
58. Inoue,K. and Takano,H. (2011) Aggravating impact of nanoparticles on immune-mediated pulmonary inflammation. *ScientificWorldJournal*, **11**, 382–390.
59. Inoue,K., Takano,H., Yanagisawa,R., Hirano,S., Sakurai,M., Shimada,A. and Yoshikawa,T. (2006) Effects of airway exposure to nanoparticles on lung inflammation induced by bacterial endotoxin in mice. *Environ. Health Perspect.*, **114**, 1325–1330.
60. Hong,E. and Dobrovolskaia,M.A. (2018) Addressing barriers to effective cancer immunotherapy with nanotechnology: achievements, challenges, and roadmap to the next generation of nanoimmunotherapeutics. *Adv. Drug. Deliv. Rev.*, doi:10.1016/j.addr.2018.01.005.
61. Kondo,S. and Sauder,D.N. (1997) Tumor necrosis factor (TNF) receptor type 1 (p55) is a main mediator for TNF-alpha-induced skin inflammation. *Eur. J. Immunol.*, **27**, 1713–1718.
62. Phillips,A., Patel,C., Pillsbury,A., Brotherton,J. and Macartney,K. (2018) Safety of human papillomavirus vaccines: an updated review. *Drug Saf.*, **41**, 329–346.
63. Miller,E.R., Lewis,P., Shimabukuro,T.T., Su,J., Moro,P., Woo,E.J., Jankosky,C. and Cano,M. (2018) Post-licensure safety surveillance of zoster vaccine live (Zostavax(R)) in the United States, Vaccine Adverse Event Reporting System (VAERS), 2006–2015. *Hum Vaccin Immunother*, **14**, 1963–1969.
64. Woo,E.J., Moro,P.L., Cano,M. and Jankosky,C. (2017) Postmarketing safety surveillance of trivalent recombinant influenza vaccine: reports to the vaccine adverse event reporting system. *Vaccine*, **35**, 5618–5621.
65. Gause,K.T., Wheatley,A.K., Cui,J., Yan,Y., Kent,S.J. and Caruso,F. (2017) Immunological principles guiding the rational design of particles for vaccine delivery. *ACS Nano*, **11**, 54–68.
66. De Gregorio,E. (2015) The path forward. *Vaccine*, **33**(Suppl. 2), B60–B63.
67. Reed,S.G., Hsu,F.C., Carter,D. and Orr,M.T. (2016) The science of vaccine adjuvants: advances in TLR4 ligand adjuvants. *Curr. Opin. Immunol.*, **41**, 85–90.
68. Hanagata,N. (2017) CpG oligodeoxynucleotide nanomedicines for the prophylaxis or treatment of cancers, infectious diseases, and allergies. *Int. J. Nanomed.*, **12**, 515–531.
69. Hong,E., Halman,J.R., Shah,A.B., Khisamutdinov,E.F., Dobrovolskaia,M.A. and Afonin,K.A. (2018) Structure and composition define immunorecognition of Nucleic Acid Nanoparticles. *Nano Lett.*, **18**, 4309–4321.
70. Davies,H., Bignell,G.R., Cox,C., Stephens,P., Edkins,S., Clegg,S., Teague,J., Woffendin,H., Garnett,M.J., Bottomley,W. *et al.* (2002) Mutations of the BRAF gene in human cancer. *Nature*, **417**, 949–954.
71. Hingorani,S.R., Jacobetz,M.A., Robertson,G.P., Herlyn,M. and Tuveson,D.A. (2003) Suppression of BRAF(V599E) in human melanoma abrogates transformation. *Cancer Res.*, **63**, 5198–5202.
72. Rackley,L., Stewart,J.M., Salotti,J., Krokhotin,A., Shah,A., Halman,J., Juneja,R., Smollett,J., Roark,B., Viard,M. *et al.* (2018) RNA fibers as optimized nanoscaffolds for siRNA coordination and reduced immunological recognition. *Adv. Funct. Mater.*, **28**, 1805959.
73. Sosman,J.A., Kim,K.B., Schuchter,L., Gonzalez,R., Pavlick,A.C., Weber,J.S., McArthur,G.A., Hutson,T.E., Moschos,S.J., Flaherty,K.T. *et al.* (2012) Survival in BRAF V600-mutant advanced melanoma treated with vemurafenib. *N. Engl. J. Med.*, **366**, 707–714.
74. Lehraiki,A., Cerezo,M., Rouaud,F., Abbe,P., Allegra,M., Kluza,J., Marchetti,P., Imbert,V., Cheli,Y., Bertolotto,C. *et al.* (2015) Increased CD271 expression by the NF-kB pathway promotes melanoma cell survival and drives acquired resistance to BRAF inhibitor vemurafenib. *Cell Discov.*, **1**, 15030.
75. Liu,J., Suresh Kumar,K.G., Yu,D., Molton,S.A., McMahon,M., Herlyn,M., Thomas-Tikhonenko,A. and Fuchs,S.Y. (2007) Oncogenic BRAF regulates beta-Trcp expression and NF-kappaB activity in human melanoma cells. *Oncogene*, **26**, 1954–1958.
76. Rosette,C. and Karin,M. (1995) Cytoskeletal control of gene expression: depolymerization of microtubules activates NF-kappa B. *J. Cell Biol.*, **128**, 1111–1119.
77. Ghosh,G., Huang,D. and Huxford,T. (2011) Recognition of nucleic acids by transcription factor NF-kB. In: Williams,M.C. and Maher,LJ III (eds). *Biological System*. Springer-Verlag, pp. 85–106.